Secondary flows over artificial bed strips

Zhi-Qian Wang, Nian-Sheng Cheng*

School of Civil and Environmental Engineering, Nanyang Technological University
Nanyang Avenue, Singapore 639798, Singapore
*Tel: +65-6790 6936; Fax: +65-6791 0676;
E-mail: cnscheng@ntu.edu.sg (N.-S. Cheng)

Abstract

Characteristics of open channel flows can be significantly modified in the presence of secondary flows. In this study, cellular secondary flows were artificially generated with alternate rough and smooth bed strips, which were aligned longitudinally in an open channel. Flow measurements were conducted with a two-dimensional Laser Doppler Anemometer system. Experimental results show that the distributions of the primary velocity and streamwise Reynolds shear stress that are altered in the presence of the secondary flows clearly deviate from those observed for two-dimensional open channel flows. The modified streamwise velocity can be represented by a function proposed in the log-wake form but varying periodically in the lateral direction. This study also demonstrates that the flow field can be linearized so that a flow quantity can be generally decomposed into two components, one being related to the average base flow and the other symbolizing the perturbation caused by the bed configuration. This perturbation-based approach finally provides an analytical description of the altered Reynolds shear stress distribution that differs from the linear profile used for two-dimensional open channel flows.

***Keywords*:**
Secondary flow; Reynolds shear stress; Velocity profile, Bed shear stress; Log-law; Open channel flow

1. Introduction

Secondary flows are ubiquitous in natural rivers and laboratory flumes. Prandtl (1952) classified secondary flows into two categories. The secondary flow of Prandtl's first kind is defined as that induced by skewing of the mean flow in curved channels or meandering rivers. Such secondary flows exist either in the laminar or turbulent conditions. Prandtl's second kind of secondary flows, also called shear- or turbulence-driven secondary flows, are those caused by the cross-sectional non-homogeneity of turbulence.

Turbulence-driven secondary flows commonly arise in straight channels or non-circular ducts. They can be initiated by the sidewall effect, free-surface effect or the variation of bed topology. In narrow open channels (e.g., width to depth ratio $B/h<5$) with immobile bed, vortices are first initiated at the corners owing to the existence of sidewalls, and then stretched and amalgamated in the lateral direction. This eventually leads to streamwise vortices in the scale of flow depth. The secondary flows so

generated are also called ‘corner flows’. In comparison, for wide channels (B/h>5), the corner vortices could damp rapidly while moving far away from the sidewalls, and therefore the central region in the channel remains free from the secondary flows. Such flow phenomena have been numerically demonstrated by Naot and Rodi (1982) for smooth boundary conditions. Nezu et al. (1985) investigated the behavior of secondary flows in smooth air ducts with different aspect ratios, and they noticed that there was no longitudinal vortex in the central region when the aspect ratio was greater than 5.

However, many geologists and hydraulic engineers (e.g. Vanoni, 1944) have inferred the existence of secondary flows in straight wide rivers from field observations such as periodic lateral variations of streamwise velocity and suspended sediment concentration. Laboratory studies done by Müller and Studerus (1979) imply that the existence of the secondary flows in wide open channels be attributed to erodible sediment beds. Colombini (1993) conducted a linear stability analysis of flow in infinitely wide channels with an erodible bed. His study indicated that the initiation of the secondary flow and sand ridges is intrinsically associated with instability of the erodible bed rather than the effect of sidewall-induced vortices.

Stable secondary flows observed in straight wide open channels can be characterized by their paired circular flow cells, of which the upflow occurs over ridges or fine-grained strips and the downflow over troughs or coarse-grained strips (Nezu and Nakagawa, 1984; McLelland et al., 1999). Because of this unique phenomenon, they are also called cellular secondary flows. Relevant experiments also suggest that the cellular secondary flows are such vortices that can be specified by channel bed conditions. The flow cells are maintained by lateral undulations either in bed roughness or in bed elevations. A number of researchers have experimentally investigated the secondary flows, but only few experiments have been conducted with attention particularly devoted to the cellular secondary flows, which are generated by fixed longitudinal ridges or strips (see Müller and Studerus, 1979; Mclean, 1981; Studerus, 1982; Nezu and Nakagawa, 1984). In these previous studies, the experiments were generally designed to verify the existence of secondary flows. The measurements demonstrated that cellular secondary flows could substantially modify the primary flow field, and the primary flow properties deviate from the theories developed for two-dimensional flows. However, it is noted that most of the results were qualitative and little work has been done to precisely evaluate the deviations induced by secondary flows. As a result, the Reynolds shear stress distribution was often misleadingly approximated to be linear either for practical uses or theoretical analyses. Similarly, the log-law was also used without validation to describe the vertical distribution of the streamwise velocity.

To further understand secondary flows induced by the lateral variations in bed roughness or bed elevation, we have recently conducted several experiments with various bed configurations (Wang et al., 2003; Wang et. al., 2004). In this paper, characteristics of the cellular secondary flows induced by bed roughness variations are first explored experimentally. The cellular secondary flows were artificially generated with a bed configuration, which comprised alternate rough and smooth strips aligned longitudinally in an open channel. Laser Doppler Anemometer

(LDA) was used to conduct detailed velocity measurements. Based on the experimental data collected, analytical formulae are then proposed for the description of vertical profiles of the streamwise velocity and Reynolds shear stress, which are modified by the secondary flows.

2. Experimental setup

The experiments were carried out in a straight rectangular tilting flume that was 18m long, 0.6m wide and 0.6m deep. The flume bed comprised nine longitudinal strips, five rough and four smooth, which were juxtaposed in an alternate fashion as shown in Fig. 1. The strip was 75mm wide each except for the two attached to the sidewalls, which was 37.5mm wide each. This layout ensured that the bed configuration was symmetrical laterally with a rough strip placed along the channel centerline. The symmetry was considered largely based on observations presented in previous studies (see Nezu and Nakagawa, 1993). The surface elevations of both rough and smooth strips were set so that the variation of the bed surface elevation was negligible. The rough strips were prepared with fine gravels packed densely, which were generally uniform with a medium diameter of 2.55mm. These sediment particles remained fixed during the experiments. The experimental conditions are summarized in Table 1. The flow discharge was $72m^3/h$ and the average velocity in the central zone of the channel was approximately 0.449m/s. The flow depth, h, was about 75mm resulting in a width-todepth ratio (B/h) of 8. Therefore, the channel was considered wide so that the flow in the central region of the channel was unaffected by the sidewalls. The mean water surface slope, J, was the same as the bed surface slope of 0.0007, and therefore the flow was considered uniform in the longitudinal direction.

Instantaneous flow velocities were measured using Laser Doppler Anemometry (LDA). A DENTEC measurement system (Flowlite 2D) was employed for this experiment, which included an integrated four-beam, two-component laser-optics unit, a correlation-type signal processor, a set of application software and other accessories. The LDA was operated in the backscatter mode. The light source was made of 10mW HeNe and 10-200mW diode-pumped frequency doubled Nd: YAG lasers that produced two red (633nm) and two green (532nm) beams respectively. A built-in 40MHz frequency shifter was equipped for distinguishing reversing flows. The laser beams passed through a 400mm-focal-length lens that was fixed on a probe with a diameter of 60mm. The sampling volume measured $0.119\times0.119\times2.51mm^3$ in the downstream (x), vertical (y), and lateral (z) directions, respectively. The LDA probe was mounted on an automated traversing system that could reposition the measurement volume within ±0.1mm in the three orthogonal directions. All the setup parameters, including the center frequency, bandwidth, maximum record length, high voltage level and gain levels, remained unchanged during the experiments, such that fluctuations in the flow characteristics among runs could be effectively reflected through real-time signal variations.

The data were collected over a half of the cross-section because of the symmetrical bed configuration, and the test section was approximately 14m downstream from the channel

entrance, where the flow was considered fully developed. Since the sidewalls can generate secondary flows that are different from those produced by bed strips, measurements were conducted both for the region near the wall and the central region so that the region that was free from the sidewall effects could be identified correctly. Two series of tests were conducted using two sets of sampling meshes. The first series was designed for measuring streamwise and vertical velocities simultaneously, while the second was to sample streamwise velocity only. The two-dimensional (2D) sampling mesh for the first series is schematically shown in Fig. 2. It had 611 measuring points located along 41 vertical lines, the latter being evenly spaced 7.5mm apart. The measurable region along different vertical lines varied, and more points were taken along the vertical lines close to the sidewall. This is because the laser beams for measuring the vertical velocity could intersect the flume bed and water surface so that they could be either obstructed by the channel bed or refracted near the fluctuating water surface. In the central part of the channel, the measurable region ranged approximately from y = 10-60mm, and the measuring points was spaced 5mm apart. More points were added to the sampling mesh for the lines near the sidewall, and 2 or 3mm vertical spacing was used for these additional points. At each position, the sampling duration was typically taken as 200s, but data collection was terminated once 20,000 sets of data were recorded. The average sampling rate was about 75Hz. The relatively long time series selected here was to enhance precision of the measurements and thus corresponding statistical computations.

One-dimensional (1D) measurements were conducted for measuring the streamwise velocity only. The data were collected for the same vertical lines as shown in Fig. 2. Each line contained 29 measuring points, and the spacing between neighboring points along each line varied. Smaller spacing was adopted near the bed because of the large velocity gradient, and the shortest distance from the measuring point to the bed was 0.5mm. The flow conditions and LDA setting parameters remained the same as those used for the 2D measurements. The sampling duration for each point was set as 200s, but the measurement was terminated once 10,000 sets of data were collected. The average sampling rate for the 1D measurements was 67Hz.

The measured instantaneous velocities were analyzed together with information of seeding particle arrival time and transit time. The data analysis yielded the mean velocities and other statistical properties. In order to picture out the mean flow pattern across the section, the sampling mesh (Fig. 2) were extended to a complete rectangular size consisting of 41×17 points, in which unknown values at additional points were extrapolated from the measured data using kriging method (McLelland et al., 1999). Because the lateral velocity component could not be measured directly, the mean lateral velocity was computed based on the continuity equation, as suggested by Nezu and Rodi (1985) and McLelland et al. (1999). As is shown subsequently, the results so computed, which may be subject to uncertainties due to relatively small values of the vertical and lateral velocities, were only used to qualitatively delineate the secondary flow cells.

3. Experimental results

Fig. 3 shows the contour maps of the normalized time-mean streamwise and vertical velocities (U/U_m and V/U_m, respectively) over the tested half section. Here U_m is the depth-averaged velocity in the central region (z/h = 0 ~ -1.0). The figure clearly demonstrates that the sidewall effect is very strong within a distance of about 1.0h from the sidewall. In this region, the maximum streamwise velocity [Fig. 3 (a)] appears below the free surface, which is phenomenally called 'velocity dip'. Beyond the near-sidewall region, say, 2.0h from the sidewall, the undulation of the mean flow field is roughly in phase with the lateral variation of the bed roughness.

The similar phenomena can also be observed from the vertical velocity contours (Fig. 3 (b)). Other high-order statistical properties computed with the same data, which are not presented here, also exhibit similar periodic variations in the lateral direction, particularly, in the central region. The central zone was approximately 4h wide, which can be considered free from the sidewall effects. For the analysis conducted subsequently, only the flow properties in the central region (z/h = 0 ~ -1.0) are considered, where a complete secondary flow cell occurred (see Fig. 4).

Due to the direct effect of the roughness elements, the near-bed streamwise velocity above the rough strips is apparently less than that above the smooth strips (Fig. 3 (a)). In contrast, the flow in the upper portion exhibits higher velocity above the rough strips and smaller velocity above the smooth strips. The maximum velocity in the central region approaches to the water surface so that the velocity dip phenomena was not clearly observed. The average velocity (U_m) occurs in the range of y/h = 0.25 - 0.5. Fig. 3 (b) shows that the downflow occurs above the rough strips while the upflow appears above the smooth strips. The maximum and minimum vertical velocities are about 0.025U_m and -0.020U_m, respectively, appearing for y/h = 0.2 - 0.4.

Using the continuity equation, i.e. $(\partial V / \partial y)+(\partial W / \partial z) = 0$, the lateral velocity ($W$) was computed from the measured vertical velocity (V). It is understood that the application of the continuity equation may cause errors due to relatively small values of lateral and vertical velocities. However, the computed lateral velocities are only used for plotting the vectors across the section. The subsequent analyses of the primary velocity and shear stress are not subject to such uncertainties. The flow vectors across the section are shown in Fig. 4(a), which clearly displays the presence of secondary flows. The mean magnitude of the velocity vectors shown in Fig. 4(a) is 0.015U_m and the largest magnitude is 0.060U_m. Based on the flow vectors, a simplified flow pattern across the section is sketched in Fig. 4(b). Near the sidewall, the circular flow comprises two triangular flow cells that are separated roughly by the corner bisector. The interaction of the two flow cells transfers the higher momentum fluid from the surface region to the bottom corner. The upflow near the sidewall brings upwards the lower momentum fluid along the sidewall. The central region is clearly characterized by the pairs of counter-rotating secondary flow cells approximately in the scale of the flow depth. At the bottom, the adjacent flow cells separate over the rough strip and reattach together over the smooth strip, and vice versa at the free surface. The ordered flow structures

illustrate that stable cellular secondary flows could be effectively induced and also maintained by the alternate rough and smooth bed strips or the lateral roughness variation.

Fig. 5 shows the contours of the dimensionless Reynolds shear stress $-\rho\overline{u'v'}/\overline{\tau_b}$, where $\overline{\tau_b}$is the average bed shear stress in the central region computed as ρghJ . It can be seen that the shear stress also varies in phase with the bed configuration. This variation will be discussed together with its theoretical analysis in the following section.

4. Analysis

The experimental results presented above clearly demonstrate that the flow structure in the presence of the secondary flow differs from that in 2D open channel flows. Regardless of this fact, the primary flow was still described in several previous studies using the formulae developed for the condition of 2D flows. For example, the primary velocity in the wall region was supposed to follow the log-law, from which the shear velocity (u_*) was derived (Studerus, 1982; Nezu and Rodi, 1985). Another example is due to Perkins (1970) and Ikeda (1981), who noted that the bed shear stress varies sinusoidally in the lateral direction, but hypothesized that the Reynolds shear stress was distributed linearly in the direction normal to the bed. Obviously, fu~~rth~~er r~~-~~esearch needs to be conducted to verify if these approximations are valid even for very restricted circumstances.

In the subsequent analysis, some basic formulations that are developed for 2D flows are first modified by including the effects of the cellular secondary flow. Analytical expressions obtained are then validated using the experimental data collected in this study and also those obtained by previous studies.

4.1. Linear approximation of the flow field

Consider a steady turbulent flow in a wide, straight open channel, of which the bed roughness varies periodically in the lateral direction. The roughness variation serves as an effective bed disturbance to generate cellular secondary flows. For comparison purposes, we define a 'base flow' as a two-dimensional uniform flow with the same values of the depth-averaged velocity, flow depth and bed slope. The flow subject to the generated secondary motion is then assumed as a result of the perturbation to the base flow due to the lateral roughness variation. This assumption is acceptable by noting that the cellular secondary flow is usually much weaker than the primary flow for the case considered in the present study. For example, the maximum velocity magnitude related to the cellular secondary flow is commonly less than 5% of that of the primary flow.

With the above consideration, the disturbed flow is further assumed as a linear superimposition of the perturbation on the base flow. Such a function was proposed by Colombini (1993) in the following form,

$$f(y,z) = f_0(y) + F(y,z) \tag{1}$$

where f is the disturbed flow quantity; f_0 is the flow quantity related to the base flow and F is the corresponding perturbation. For the case of the periodic perturbation, the flow characteristics appear in the sinusoidal mode laterally, as is demonstrated by the experimental results. Therefore, Eq. (1) can be rewritten as

$$f(y,z) = f_0(y) + f_1(y)G(z) \tag{2}$$

where $f_1(y)$ is the amplitude of the perturbation; and G(z) is a periodic function. As is shown later, the periodic function can be taken as cosine to characterize the lateral distributions of the streamwise velocity and Reynolds shear stress for the present study. In addition, it is also assumed that perturbations higher than the first-order are negligible.

4.2. Distribution of primary velocity

First, the log-law is used to represent the profile of the primary velocity related to the base flow, i.e.

$$\frac{\kappa U_0(y)}{\overline{u_*}} = \ln\frac{y}{R_0} \tag{3}$$

where U_0 is the streamwise velocity for the base flow; $\overline{u_*}$ is the average shear velocity; κ is the von Karman coefficient (= 0.4); and R_0 is the zero-velocity level or hydrodynamic roughness length for the base flow. In the presence of the cellular secondary flows, the distribution of the primary velocity U would deviate from Eq. (3). This can be examined in detail using the experimental data.

Fig. 6 plots the primary velocity profiles measured at eleven locations (z/h = 0.0, -0.1, - 0.2 ... -1.0). For comparison, two profiles are plotted together, one being sampled over the rough strip and the other over the smooth strip, and they are located at the same distance measured laterally from the strip interface (z/h = -0.5). The two profiles show different variations; they generally curve down over the rough strip but bend up over the smooth strip. It can also be observed that in the lower portion of the flow, the velocity gradient over the rough strip is much steeper than that over the smooth strip. In particular, the profile measured at the strip interface (z/h = -0.5) can be approximated as a straight line. Similar results were also reported by Nakagawa et al. (1981), which are reproduced in Fig. 7.

Given the above properties of the velocity profile, it seems possible to apply the log-law in the presence of the secondary flows provided that the associated variations are effectively taken into account. As a first approximation, the log-law is modified to be

$$\frac{\kappa U(y)}{\overline{u_*}} = a_1 \ln\frac{y}{R} + a_2 \sin^2\frac{\pi y}{2h} \tag{4}$$

where R is the zero-velocity level used for the logarithmic term; and a_1 and a_2 are the parameters used to include the effect of the secondary flows. Eq. (4) appears to be similar to the conventional log-wake function. However, some differences should be emphasized here. First, the two parameters, a_1 and a_2, are largely related to the perturbation-induced variations. Second, the term,$a_2\sin^2[\pi y/(2h)]$, is proposed only to empirically account for the curvature of the velocity profile induced by the secondary flow. In other words, Eq. (4) would reduce to Eq. (3) if the effect of the secondary flow is not considerable.This holds at z/h = - 0.5, where the measured velocity profile looks like a straight line, as shown in Fig. 6. Therefore, for this particular case, we can take a_1=1 and a_2=0.

Furthermore, a shear velocity (denoted by $\overline{u_{*(2)}}$) can be deduced by fitting Eq. (4) with a_1=1 and a_2=0 to the velocity profile measured at z/h = - 0.5. The curve fitting gives that $\overline{u_{*(2)}} = 0{:}024$ m/s and the zero-velocity level (R_0) = 1.8×10^{-5} m. It is interesting to note that this shear velocity is very close to that evaluated based on the bed slope, i.e., $\overline{u_{*(1)}} = \sqrt{ghJ} = 0.023$ m/s. This is reasonable because of the insignificant secondary flow effect observed at the transitional location (z/h = -0.5).

To examine how the velocity distribution deviates from the straight line due to the secondary flow, each individual profiles will be compared to that measured at z/h = -0.5. This can be simply done by fitting Eq. (4) to each profile by varying a_1 and a_2, as shown in Fig. 6. The approach used here also implies that the flow properties obtained at z/h = -0.5 is equivalent to those associated with the base flow. Fig. 6 clearly demonstrates that the measured velocity profiles, which are modified by the secondary flow, can be acceptably described using Eq. (4). To perform the curve fitting, Eq. (4) is re-written as

$$\frac{\kappa U(y)}{\overline{u_*}} = a_1 \ln\frac{y}{R_0} + a_2\sin^2\frac{y\pi}{2h} + a_1 \ln\frac{R_0}{R} \tag{5}$$

where the two coefficients, a1 and a_2 and the term of a_1 $\ln(R_0/R)$ are optimized for each particular profile. The computed results show that the values of a1, a_2 and a_1 $\ln(R_0/R)$ generally vary in the lateral direction, as plotted in Fig. 8. The variations are periodic and can be described using the cosine function as follows

$$a_1 = 1 + \delta_1 \cos\frac{\pi z}{\lambda} \tag{6}$$

$$a_2 = \delta_2 \cos\frac{\pi z}{\lambda} \tag{7}$$

$$a_1 \ln\frac{R_0}{R} = D\cos\frac{\pi z}{\lambda} \tag{8}$$

where $\delta_1 \approx 0.3$; $\delta_2 \approx -0.8$; $D \approx -1.7$ and λ(= 7.5cm) is the half wavelength associated with the bed configuration.

To further examine the velocity profile obtained above with the concept of the linearization given by Eq. (2), U is decomposed into two components, one representing the base-flow and the other being related to its lateral undulation, i.e.

$$U(y,z) = U_0(y) + U_1 \cos\frac{\pi z}{\lambda} \tag{9}$$

where U_1 is the amplitude of the lateral velocity undulation. Substituting Eq. (9) together with Eq. (3) into Eq. (4) yields

$$\frac{\kappa U_1(y)}{\overline{u_*}} \cos\frac{\pi z}{\lambda} = (a_1 - 1)\ln\frac{y}{R_0} + a_1 \ln\frac{R_0}{R} + a_2 \sin^2\frac{\pi y}{2h} \tag{10}$$

Substituting Eqs. (6) to (8) into Eq. (10), we get

$$U_1(y) = \frac{\overline{u_*}}{\kappa}\left(\delta_1 \ln\frac{y}{R_0} + D + \delta_2 \sin^2\frac{\pi y}{2h}\right) \tag{11}$$

Finally, for the primary velocity, in the form of Eq. (2), Eq. (9) can be re-written as

$$\frac{U(y,z)}{\overline{u_*}} = \frac{1}{\kappa}\ln\frac{y}{R_0} + \frac{1}{\kappa}\left(\delta_1 \ln\frac{y}{R} + D + \delta_2 \sin^2\frac{\pi y}{2h}\right)\cos\left(\frac{\pi z}{\lambda}\right) \tag{12}$$

Eq. (12) shows the modification of the logarithmic distribution of the streamwise velocity due to the presence of the cellular secondary flow.

4.3. Streamwise Reynolds shear stress

In this study, the eddy viscosity concept is assumed to be applicable to the streamwise Reynolds shear stress. Therefore, the Reynolds shear stress $-\rho\overline{u'v'}$ can be related to the gradient of the streamwise velocity as

$$-\rho\overline{u'v'} = \rho\nu_t \frac{\partial U}{\partial y} \tag{13}$$

in which ρ is the density of fluid; and ν_t is the eddy viscosity. Following the approach given by Eq. (2), ν_t can be further approximated to be

$$\nu_t = \nu_{t0} + \nu_{t1} \cos\frac{\pi z}{\lambda} \tag{14}$$

where ν_{t0} is the eddy viscosity related to the base flow; and ν_{t1} is the amplitude of the viscosity perturbation. Substituting Eqs. (9) and (14) into Eq. (13) and ignoring the second-order perturbation yields

$$-\overline{u'v'} = v_{t0}\frac{\partial U_0}{\partial y} + \left(v_{t0}\frac{\partial U_1}{\partial y} + v_{t1}\frac{\partial U_0}{\partial y}\right)\cos\frac{\pi z}{\lambda} \tag{15}$$

Eq. (15) indicates that the lateral variation of $-\overline{u'v'}$ depends on the perturbations induced by the primary velocity and the eddy viscosity, respectively.

Furthermore, consider that the eddy viscosity can also be modelled using the mixing length, l,

$$v_t = l^2\frac{\partial U}{\partial y} \tag{16}$$

The mixing length l is decomposed into two components as

$$l = l_0 + l_1\cos\frac{\pi z}{\lambda} \tag{17}$$

where l_0 is the mixing length for the base flow; and l_1 is the amplitude of the mixing length perturbation. Substituting Eqs. (9), (14), and (17) into Eq. (16) and ignoring perturbation terms higher than the first-order yields

$$\frac{v_{t1}}{v_{t0}} = \frac{\partial U_1/\partial y}{\partial U_0/\partial y} + 2\frac{l_1}{l_0} \tag{18}$$

where v_{t0} is taken as $l_0^{2(}\partial U_0/\partial y)$ for the base flow. Noting that - $\overline{u'v'} = \overline{u_*}^2(1-y/h)$ for the base flow, with Eqs. (3), (11) and (18), Eq. (15) can be re-written as

$$\frac{-\overline{u'v'}}{\overline{u_*}^2} = \left(1-\frac{y}{h}\right)\left[1+\left(\delta_3+\delta_4\frac{y}{h}\sin\frac{\pi y}{h}\right)\cos\frac{\pi z}{\lambda}\right] \tag{19}$$

where $\delta_3 = 2\,\delta_1 + 2l_1/l0$ and $\delta_4 = \pi\,\delta_2$. Obviously, these two coefficients are associated with the amplitude of the shear stress undulation.

To compare with the measured shear stress profiles, Eq. (19) is rearranged in the following form, which is similar to Eq. (4) proposed for the primary velocity,

$$\frac{-\overline{u'v'}}{\overline{u_*}^2} = a_3\left(1-\frac{y}{h}\right) + a_4\left(1-\frac{y}{h}\right)\frac{y}{h}\sin\frac{\pi y}{h} \tag{20}$$

where $a_3 = 1+\delta_3\cos(\pi z\lambda)$ and $a_4 = \delta_4\cos(\pi z\lambda)$. Plotted in Fig. 9 are the distributions of $-\overline{u'v'}$ measured at z/h = 0.0, -0.1, -0.2 ... -1.0. The shear stress profile

at z/h = -0.5, where the secondary is insignificant, is first fitted to Eq. (20) with a_3=1 and a_4=0. Then, the bed shear shear stress $\rho\overline{u^2}$ is estimated by extrapolating the shear stress profile to the bed surface, which yields that the shear velocity denoted by $\overline{u_*}_{(3)}$ is 0.0215 m/s. As shown in Table 1, this shear velocity is close to those evaluated from the velocity profile and the bed slope, respectively. Fig. 9 demonstrates that the measured shear stress profiles can be well represented by Eq. (20). The deviation of $-\overline{u'v'}$ from the linear distribution that is associated with the base flow appears differently over the different bed strips. Higher shear stresses occur in the upper flow portion above the smooth strip, whereas the shear stress becomes smaller over the rough strip for $y/h > 0.2$. Near the bed, however, the values of $-\overline{u'v'}$ over the smooth strip tend to be smaller than those over the rough strip.

The coefficients, a_3 and a_4, are taken to be constant when fitting Eq. (20) to each shear stress profile measured. Their values are plotted in Fig. 10, showing that the variations of the two parameters can be approximated by the cosine relationships, $a_3 = 1 + \delta_3 \cos(\pi z\lambda)$ and $a_4 = 1 + \delta_4 \cos(\pi z\lambda)$, with δ_3 = 0.18 and δ_4 = -1.44. This further confirms that Eq.(19) is generally applicable to the description of the distribution of the streamwise Reynolds shear stress that is affected by the cellular secondary flows.

In addition, Eq. (20) is also compared favorably with the experimental results for air flows that were collected by Nakagawa et al. [7] and Nezu and Nakagawa [9], as presented in Fig. 11. For Nakagawa et al's [7] case, the flow depth (h) was measured from the channel bed to the position where the maximum velocity occurred, which is different from that used in their original work. As mentioned previously, cellular secondary flows could be generated in a straight channel either with longitudinal ridges (lateral variations in bed elevation) or rough/ smooth strips (lateral variations in bed roughness). In spite of the two different bed configurations, the flows could still demonstrate some similarities. Colombini and Parker (1995) have shown that these flows could be examined in quite similar approaches, which were developed based on the concept of mixing length. They also reported that the vertical structure of the mixing length played an important role in deciding the direction of flow cell rotation. In the further study, we will explore how the considerations presented in this paper could be extended to the case of secondary flows induced by lateral variations in the bed elevation.

4.4. Streamwise bed shear stress

The primary bed shear stresses at different locations are obtained by extrapolating the corresponding profiles of $-\overline{u'v'}$ to the bed surface. Fig. 12 shows that the lateral distribution of the bed shear stress can be described by the following cosine function,

$$\frac{\tau_b}{\rho\overline{u_*}^2} = \frac{u_*^2}{\overline{u_*}^2} = 1 + \delta_b \cos\frac{\pi z}{\lambda} \tag{21}$$

Where $\tau_b (= \rho u_*^2)$ is the local bed shear stress; and $\delta_b \approx 0.18$. It should be mentioned that some empirical formulae in the form similar to Eq. (21) have been

previously proposed by Perkins (1970) and Ikeda (1981) for describing the bed shear stress variation in the presence of cellular secondary flows.

Since the profile of the streamwise velocity may deviate noticeably from the log-law in the presence of secondary flows, it is clear that an estimate of the bed shear stress by fitting the measured velocity distribution to the log-law would generate misleading results. However, this was not clarified in the previous studies. For example, Nakagawa et al. (1981) and Studerus (1982) both evaluated the bed shear stress by applying log-law to the measured streamwise velocity profiles in spite of the presence of cellular secondary flows.

5. Conclusions

Turbulent open channel flows over alternate rough and smooth strips aligned longitudinally were measured using Laser Doppler Anemometer. The measurements show that secondary flow induced comprises corner vortices near the sidewall and the cellular motions in the central region of the channel. The cellular flow cell is characterized by the downflow occurring above the rough strips and the upflow over the smooth strips. Lateral distributions of the primary velocity and Reynolds shear stress are generally not uniform but vary with the secondary flow structure. The experimental results confirm that it is the non-uniformity of turbulence near the bed that generates secondary flows, and in turn, because of the secondary motion, turbulent characteristics of the primary flow are redistributed across the section.

Subject to the secondary flow, the vertical profile of the primary velocity generally deviates from the log-law. The deviation is considerable, in particular, for the region where the upflow or downflow prevails. The modified vertical profile of the primary velocity is represented in this study by a function in the log-wake style, while its lateral periodic variation is delineated by a cosine function with a wave length specified by the bed configuration.

Considering that the secondary flow is much weaker than the primary flow, the flow field is linearized so that a flow quantity can be reasonably decomposed into two components, one being related to the average base flow and the other symbolizing the perturbation caused by the bed configuration. The application of this approach leads to an analytical formulation of the Reynolds shear stress distribution that due to secondary flows significantly differs from the linear profile applicable for 2D open channel flows. The bed shear stress, which is evaluated based on the extrapolation of the Reynolds shear stress distribution, exhibits regular undulations in the lateral direction that are clearly dominated by the specified bed configuration.

It should be mentioned that the formulae proposed for describing the distributions of the streamwise velocity and shear stress may be only applicable for limited bed and flow conditions. Further studies need to be done to generalize the analysis and also to extend it to the case of secondary flows that are induced by lateral variations in the bed elevation.

References

[1] Colombini M. Turbulence driven secondary flows and the formation of sand ridges. J Fluid Mech 1993;254:701–19.

[2] Colombini M, Parker G. Longitudinal streaks. J Fluid Mech 1995;304:161–83. Ikeda S. Self-formed straight channels in sandy bed. ASCE, J Hydraulic Div 1981;107:389-406

[3] Mclean SR. The role of non-uniform roughness in the formation of sand ribbons. Mar Geol 1981;42:49–74.

[4] McLelland SJ, Ashworth PJ, Best JL, Livesey JR. Turbulence and secondary flow over sediment strips in weakly bimodal bed material. ASCE, J Hydraulic Eng 1999;125(5):463–73.

[5] Müller A, Studerus X. Secondary flow in an open channel. In: Proc of 18th IAHR Congress. Cagliari, Italy. 1979;3:19–24.

[6] Nakagawa H, Nezu I, Tominaga A. Turbulent structure with and without cellular secondary currents over various bed configurations. Annuals (in Japanese). Disaster Prevention Research Institute, Kyoto University, 1981;24B:315–38.

[7] Naot D, Rodi W. Calculation of secondary currents in channel flow. ASCE, J Hydraulic s Div 1981;108:948–68.

[8] Nezu I, Nakagawa H. Cellular secondary currents in straight conduit. ASCE, J Hydraulic Eng 1984;110:173–93.

[9] Nezu I, Nakagawa H. Turbulence in open channels. IAHR/AIRH Monograph. Balkema, Rotterdam, The Netherlands; 1993.

[10] Nezu I, Rodi W, Experimental study on secondary currents in open channel flows. In: Proc of 21st IAHR Congress; 1985. p. A125–32.

[11] Nezu I, Nakagawa H, Tominaga A. Secondary currents in a straight channel flow and the relation to its aspect ratio. Turbulent Shear Flows IV. Springer; 1985. p. 246–60.

[12] Perkins HJ. The formation of streamwise vorticity in turbulent flow. J Fluid Mech 1970;44:721–44.

[13] Prandtl L. Essentials of fluid dynamics. New York, US: Hafner Publishing Company; 1952.

[14] Studerus X. Sekund*ä*rstr*ö*mungen im offenen Gerinne über rauhen L*ä*ngsstreifen, Ph.D. Thesis, Institut fü r Hydromechanik und Wasserwirtschaft, ETH, Zürich, Switzerland. 1982.

[15] Vanoni VA. Transportation of suspended sediment by water. Trans ASCE 1944;111:67–133.

[16] Wang ZQ, Cheng NS, Chiew YM, Chen XW. Secondary flows in open channel with smooth and rough bed strips. In: Proc of 30th IAHR Congress, Thessaloniki, Greece, Theme C. 2003;1:111–8.

[17] Wang ZQ, Cheng NS, Chiew YM. Measurement of cellular secondary flow over a longitudinally ridged bed. Proc of Second Int Conf on Erosion and Sedimentation, 2. Singapore: Stallion Press; 2004. p. 391–8.–406. material. ASCE, J Hydraulic Eng 1999;125(5):463–73.

Nomenclature

a_1, a_2	parameters used in the function for U
a_3, a_4	parameters used in the function for $-\overline{u'v'}$
B	channel width
D	parameter used in the function for U
f	flow quantity subject to secondary flows
f_0	flow quantity related to the base flow
f_1	amplitude of the lateral variation
F	perturbation term
G	periodic function in the lateral direction
g	gravitational acceleration
h	flow depth
J	bed slope
l	mixing length
l_0	mixing length related to the base flow
l_1	amplitude of the lateral variation of the mixing length
Q	total discharge
R	zero-velocity level for the logarithmic term
R_0	zero-velocity level related to the base flow
U_0	streamwise velocity related to the base flow
U_1	amplitude of the lateral variation of the streamwise velocity
U_m	depth-averaged streamwise velocity in the central zone
u_*	local shear velocity
$\overline{u_*}$	average shear velocity in the central zone
u, v	instantaneous flow velocities in the streamwise and vertical directions
u', v'	velocity fluctuations in the streamwise and vertical directions
U, V, W	time-averaged flow velocities in the streamwise, vertical and lateral directions
y, z	vertical and lateral coordinates
δ_1, δ_2	coefficients used in the function for U
δ_3, δ_4	coefficients used in the function for $-\overline{u'v'}$
δ_b	amplitude of the perturbation in the bed shear stress
κ	von Karman constant (=0.4)
λ	strip width in the central zone of the channel
ν	kinematic viscosity of fluid
ν_t	eddy viscosity
ν_{t0}	eddy viscosity associated with the base flow
ν_{t1}	amplitude of the lateral variation of the eddy viscosity
ρ	fluid density
τ_b	local bed shear stress
$\overline{\tau_b}$	average bed shear stress ($=\rho g h J$)
$-\rho\overline{u'v'}$	streamwise Reynolds shear stress

List of Figures

List of tables

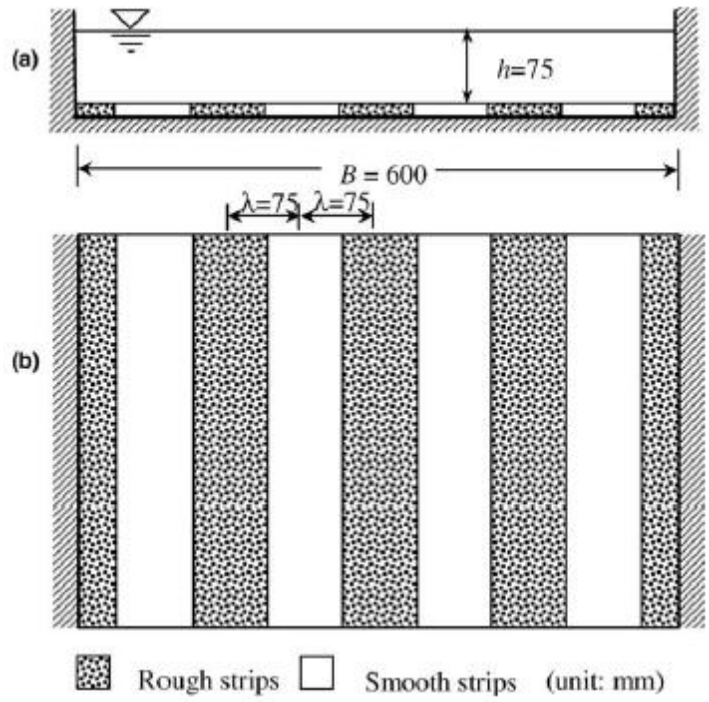

Figure 1

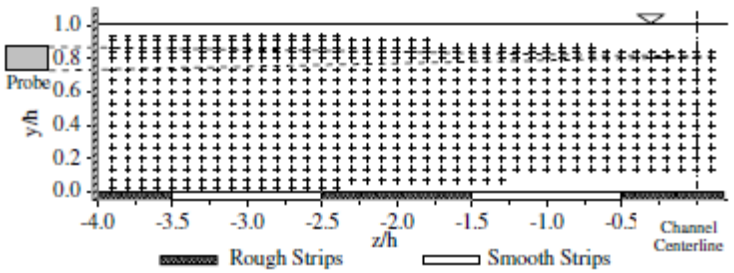
1.0
0.8
Probe
0.6
y/h
0.4
0.2
0.0
-4.0
-3.5
-3.0
-2.5
-2.0
-1.5
-1.0
-0.5
z/h
Channel
Centerline
Rough Strips
Smooth Strips

Figure 2

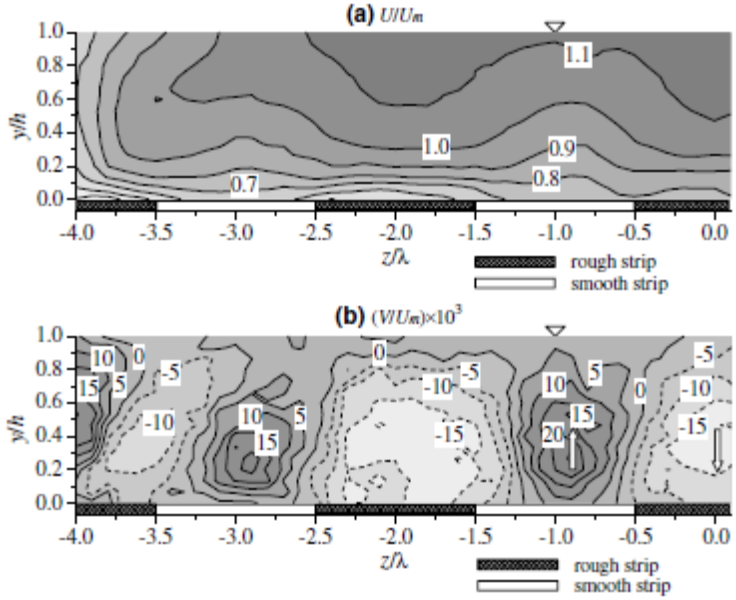
(a) U/Um
1.0
0.8
0.6
0.4
0.2
0.0
y/h
1.1
1.0
0.9
0.8
0.7
-4.0
-3.5
-3.0
-2.5
-2.0
-1.5
-1.0
-0.5
0.0
z/λ
rough strip
smooth strip
(b) (V/Um)×10^3
10
0
-5
15
5
-10
10
5
15
0
-5
-10
5
-10
15
20
0
-5
-10
-15
rough strip
smooth strip

Figure 3

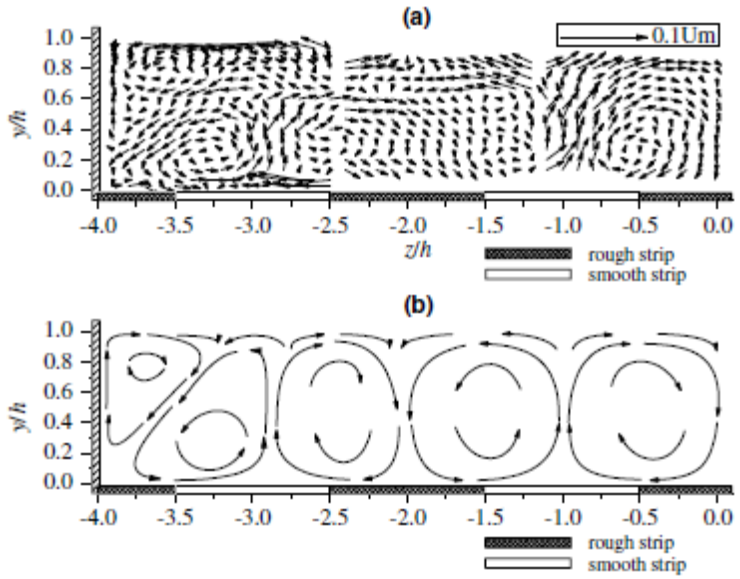
(a)
0.1Um
1.0
0.8
0.6
0.4
0.2
0.0
y/h
-4.0
-3.5
-3.0
-2.5
-2.0
-1.5
-1.0
-0.5
0.0
z/h
rough strip
smooth strip
(b)
1.0
0.8
0.6
0.4
0.2
0.0
y/h
-4.0
-3.5
-3.0
-2.5
-2.0
-1.5
-1.0
-0.5
0.0
rough strip
smooth strip

Figure 4

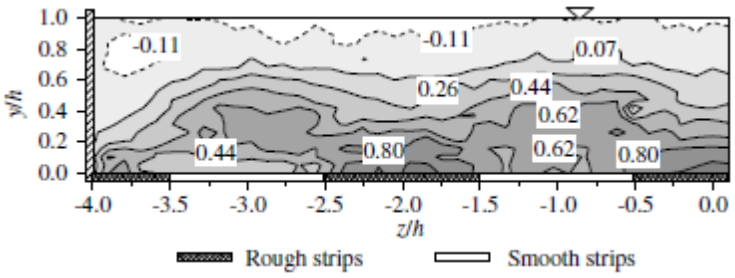
1.0
0.8
0.6
0.4
0.2
0.0
y/h
-0.11
-0.11
0.07
0.26
0.44
0.62
0.44
0.80
0.62
0.80
-4.0
-3.5
-3.0
-2.5
-2.0
-1.5
-1.0
-0.5
0.0
z/h
Rough strips
Smooth strips

Figure 5

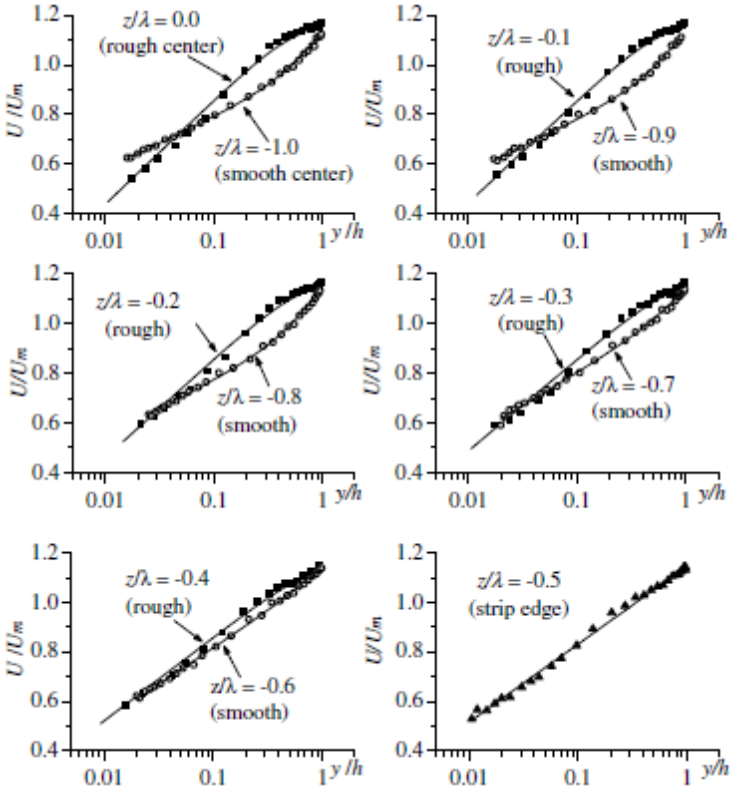
z/λ = 0.0
(rough center)
z/λ = -1.0
(smooth center)
z/λ = -0.1
(rough)
z/λ = -0.9
(smooth)
z/λ = -0.2
(rough)
z/λ = -0.8
(smooth)
z/λ = -0.3
(rough)
z/λ = -0.7
(smooth)
z/λ = -0.4
(rough)
z/λ = -0.6
(smooth)
z/λ = -0.5
(strip edge)
U /Um
y /h
1.2
1.0
0.8
0.6
0.4
0.01
0.1
1

Figure 6

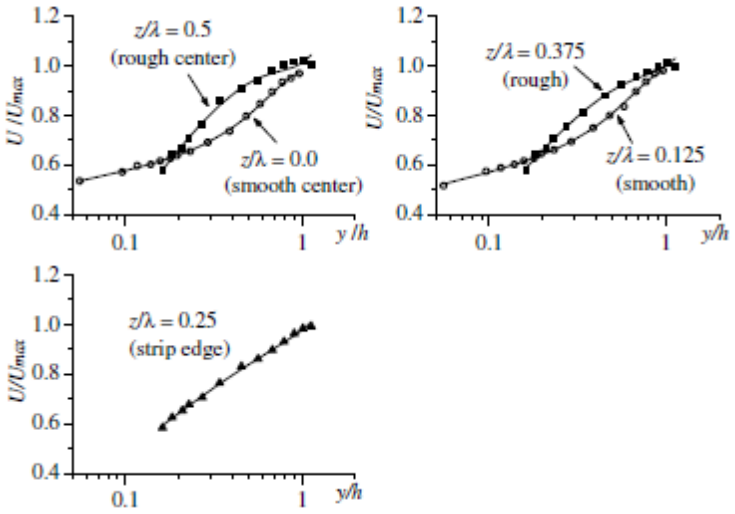
1.2
1.0
0.8
0.6
0.4
U /U_max
z/λ = 0.5
(rough center)
z/λ = 0.0
(smooth center)
0.1
1
y /h
z/λ = 0.375
(rough)
z/λ = 0.125
(smooth)
y/h
z/λ = 0.25
(strip edge)

Figure 7

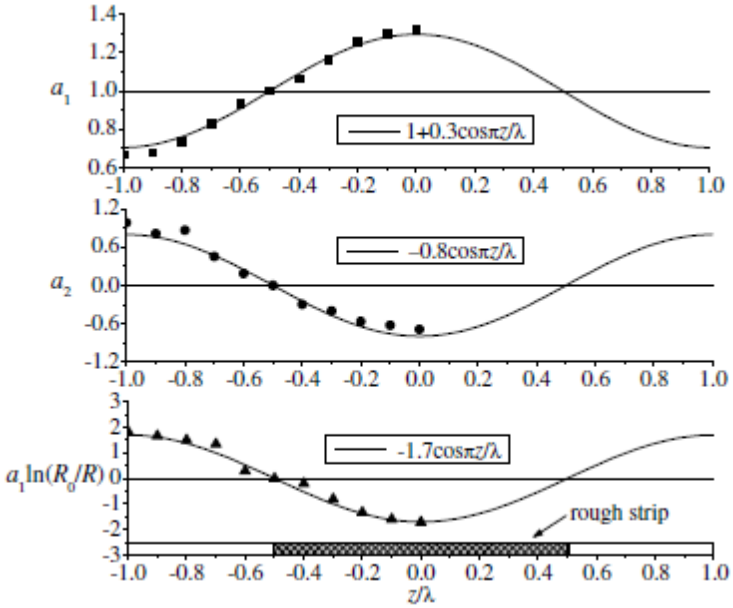

Figure 8

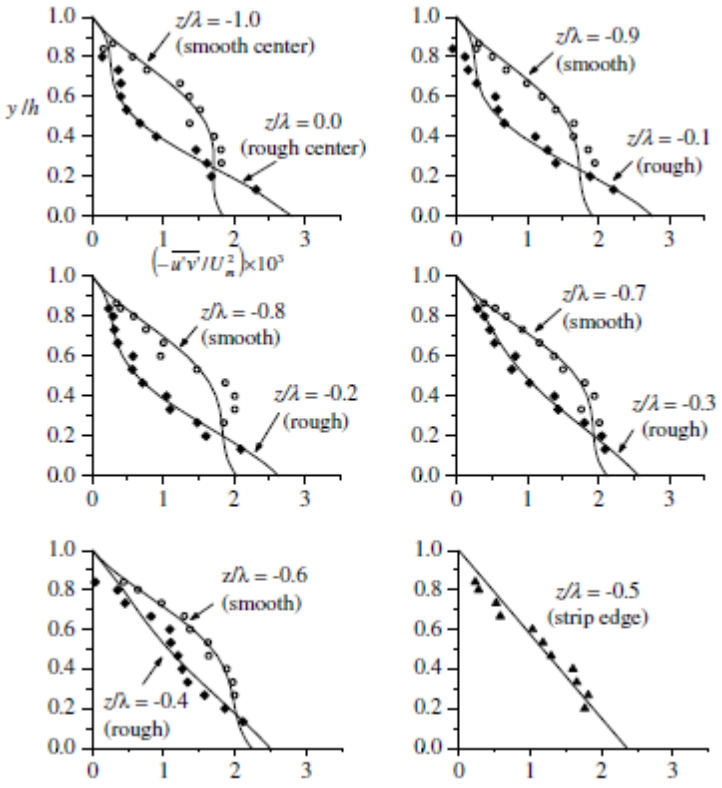
y /h
z/λ = -1.0
(smooth center)
z/λ = 0.0
(rough center)
z/λ = -0.9
(smooth)
z/λ = -0.1
(rough)
z/λ = -0.8
(smooth)
z/λ = -0.2
(rough)
z/λ = -0.7
(smooth)
z/λ = -0.3
(rough)
z/λ = -0.6
(smooth)
z/λ = -0.4
(rough)
z/λ = -0.5
(strip edge)
$\left(-\overline{u'v'}/U_a^2\right)\times10^3$

Figure 9

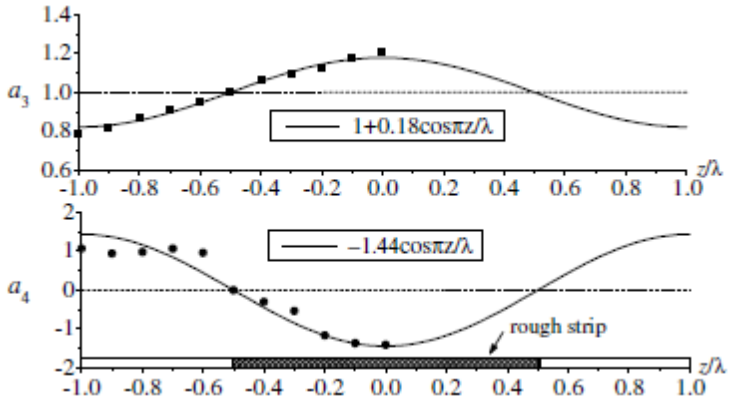
1.4
1.2
a_3 1.0
0.8
0.6
1+0.18cosπz/λ
-1.0 -0.8 -0.6 -0.4 -0.2 0.0 0.2 0.4 0.6 0.8 1.0
z/λ
2
1
a_4 0
-1
-2
−1.44cosπz/λ
rough strip
-1.0 -0.8 -0.6 -0.4 -0.2 0.0 0.2 0.4 0.6 0.8 1.0
z/λ

Figure 10

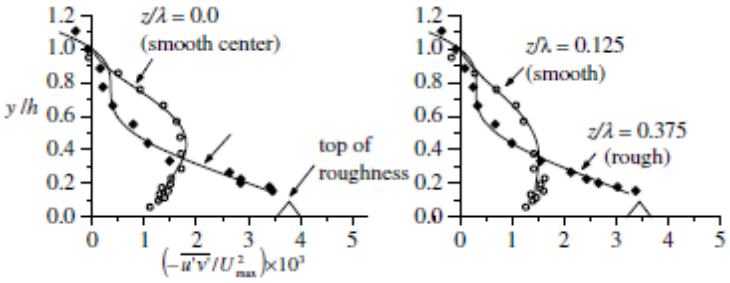
z/λ = 0.0
(smooth center)
top of
roughness
z/λ = 0.125
(smooth)
z/λ = 0.375
(rough)
y /h
1.2
1.0
0.8
0.6
0.4
0.2
0.0
0
1
2
3
4
5
$\left(-\overline{u'v'}/U_{max}^2\right)\times10^3$

Figure 11

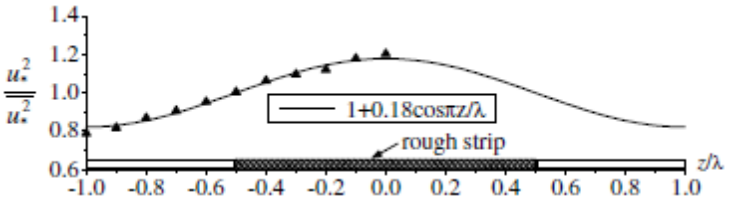
1.4
1.2
1.0
0.8
0.6
$\frac{u_*^2}{\overline{u_*^2}}$
1+0.18cosπz/λ
rough strip
z/λ
-1.0
-0.8
-0.6
-0.4
-0.2
0.0
0.2
0.4
0.6
0.8
1.0

Figure 12

Flow parameter	Value
Channel width, B	0.6 m
Mean depth, h	0.075 m
Channel aspect ratio, B/h	8
Hydraulic radius, R_h	0.06 m
Total discharge, Q	72 m^3/h
Average streamwise velocity in the central zone, U_m	0.449 $m\,s^{-1}$
Bed surface slope, J	0.0007
Water temperature	30 °C
Kinematic viscosity, ν	$8.0 \times 10^{-7}\ m^2\,s^{-1}$
Average bed shear stress, $\overline{\tau_b} = \rho g R_h J$	0.515 Nm^{-2}
Average shear velocity	
$\overline{u_*}_{(1)} = \sqrt{gJh}$	0.0227 $m\,s^{-1}$
$\overline{u_*}_{(2)}$ estimated using velocity profile at $z/h = -0.5$	0.0240 $m\,s^{-1}$
$\overline{u_*}_{(3)}$ estimated using Reynolds shear stress profile at $z/h = -0.5$	0.0215 $m\,s^{-1}$
Froude number, $U_m/\sqrt{gh}$	0.523
Reynolds number, $U_m h/\nu$	42,000

Table 1